Phase transition-induced band edge engineering of $BiVO_4$ to split pure water under visible light

Won Jun Jo[a,1], Hyun Joon Kang[b,1], Ki-Jeong Kong[c], Yun Seog Lee[d], Hunmin Park[b], Younghye Lee[b], Tonio Buonassisi[d], Karen K. Gleason[a], and Jae Sung Lee[e,2]

[a]Department of Chemical Engineering, Massachusetts Institute of Technology, Cambridge, MA 02139; [b]Department of Chemical Engineering, Pohang University of Science and Technology, Pohang 790-784, Korea; [c]Korea Institute of Chemical Technology, Daejeon 305-343, Korea; [d]Department of Mechanical Engineering, Massachusetts Institute of Technology, Cambridge, MA 02139; and [e]School of Energy and Chemical Engineering, Ulsan National Institute of Science and Technology, Ulsan 689-798, Korea

Edited by Alexis T. Bell, University of California, Berkeley, CA, and approved September 18, 2015 (received for review May 18, 2015)

Through phase transition-induced band edge engineering by dual doping with In and Mo, a new greenish $BiVO_4$ ($Bi_{1-X}In_XV_{1-X}Mo_XO_4$) is developed that has a larger band gap energy than the usual yellow scheelite monoclinic $BiVO_4$ as well as a higher (more negative) conduction band than H^+/H_2 potential [0 V_{RHE} (reversible hydrogen electrode) at pH 7]. Hence, it can extract H_2 from pure water by visible light-driven overall water splitting without using any sacrificial reagents. The density functional theory calculation indicates that In^{3+}/Mo^{6+} dual doping triggers partial phase transformation from pure monoclinic $BiVO_4$ to a mixture of monoclinic $BiVO_4$ and tetragonal $BiVO_4$, which sequentially leads to unit cell volume growth, compressive lattice strain increase, conduction band edge uplift, and band gap widening.

photocatalysis | water splitting | band edge engineering | bismuth vanadate | dual doping

Photocatalytic water splitting with a particulate semiconductor powered by sunlight is an ideal route to cost-effective, large-scale, and sustainable hydrogen production because of its extreme simplicity. However, it is challenging, because it requires a rare photocatalyst that carries a combination of suitable band gap energy, appropriate band positions, and photochemical stability (1–5). Thus, reproducible photocatalytic systems for visible light-driven overall water splitting (OWS) by one-step photoexcitation are also rare, although there were several reports of such systems (4–6). In the best-known successful case, Domen and coworkers (5) reported in 2005 that a solid solution of GaN and ZnO [$(Ga_{1-x}Zn_x)(N_{1-x}O_x)$] was a stable photocatalyst that could split water into H_2 and O_2 under visible light when modified with a cocatalyst. This system remains the most active and reproducible one-step OWS photocatalyst responsive to visible light so far (4).

Scheelite monoclinic (*m*-) $BiVO_4$ is a well-documented photocatalyst having suitable band gap energy ($E_g \sim 2.4$ eV) for absorbing visible light (7–10). Also, it is chemically stable in aqueous solution under light irradiation. Thus, it functions as an excellent photocatalyst for O_2 evolution under visible light in the presence of an appropriate electron acceptor (e.g., $AgNO_3$). However, because the bottom of its conduction band is located at a more positive potential than the potential of water reduction [0 V_{RHE} (reversible hydrogen electrode) at pH 7], it is incapable of evolving H_2. In addition, it shows poor charge transport characteristics (11) and weak surface adsorption properties (12), causing low photocatalytic activity. To overcome these weaknesses, a variety of strategies, such as heterojunction structure formation (11, 13, 14), loading cocatalysts (8, 15–17), and impurity doping (1, 7, 12, 18–23), has been attempted. These strategies were successful in improving $BiVO_4$'s oxidation capability for photoelectrochemical water oxidation (1, 11, 13, 15, 19, 24–28) as well as the *Z* scheme (two-photon excitation) water splitting system (29). Also, cocatalyzed $Bi_xY_{1-x}VO_4$ ($x \sim 0.5$) (7, 8) and cocatalyzed $Bi_{0.5}La_{0.5}VO_4$ (23) promoted OWS by raising the conduction band edge (CBE) position, but OWS under visible light irradiation over $BiVO_4$-based photocatalysts has not been fully shown.

To meet this challenge, we developed greenish $BiVO_4$ ($GBVO_x$; x = atom ratio of In and Mo), $Bi_{1-x}In_xV_{1-x}Mo_xO_4$, by simultaneously substituting In^{3+} for Bi^{3+} and Mo^{6+} for V^{5+} in the host lattice of *m*-$BiVO_4$. The new $GBVO_x$ photocatalyst has a slightly larger band gap energy than the usual yellow scheelite *m*-$BiVO_4$ as supported by the unique color change to green and a higher (more negative) conduction band than H^+/H_2 potential (0 V_{RHE} at pH 7). Consequently, as depicted in Fig. 1, $GBVO_x$ is able to split water into H_2 and O_2 under visible light irradiation without using any sacrificial reagents (e.g., CH_3OH or $AgNO_3$). Herein, we report the dual-metal doping effects on the optical absorption behavior, crystal structure, and electronic band structure of $BiVO_4$, which led to one-photon OWS under visible light irradiation. We elucidate the physical origin of the augmented photoresponse behaviors of $GBVO_x$ through density functional theory (DFT) calculation of electronic structure as well as a variety of physical and electrochemical characterizations.

Results and Discussion

Physical Properties of $GBVO_x$. The magnified X-ray diffraction (XRD) patterns of pristine $BiVO_4$ and four $GBVO_x$ samples with different target atom ratios (x = 0.02, 0.05, 0.10, and 0.15) are shown in Fig. 2*A* (more details are in *SI Appendix*, Fig. S1 *A–D*) to identify the evolution of the crystal structure by doping.

Significance

Hydrogen has been recognized as one of the most promising energy carriers for the future, because it can generate enormous energy by clean combustion chemistry without any greenhouse gas emissions. Water splitting under visible light irradiation is an ideal route to cost-effective, large-scale, and sustainable hydrogen production, but it is challenging, because it requires a rare photocatalyst that carries a combination of suitable band gap energy, appropriate band positions, and photochemical stability. To create this rare photocatalyst, we engineered the band edges of $BiVO_4$ by simultaneously substituting In^{3+} for Bi^{3+} and Mo^{6+} for V^{5+} in the host lattice of monoclinic $BiVO_4$, which induced partial phase transformation from pure monoclinic $BiVO_4$ to a mixture of monoclinic $BiVO_4$ and tetragonal $BiVO_4$.

Author contributions: K.K.G. and J.S.L. designed research; W.J.J., H.J.K., K.-J.K., and Y.S.L. performed research; K.-J.K., Y.S.L., H.P., Y.L., and T.B. contributed new reagents/analytic tools; W.J.J., H.J.K., and H.P. analyzed data; and W.J.J. and J.S.L. wrote the paper.

The authors declare no conflict of interest.

This article is a PNAS Direct Submission.

[1]W.J.J. and H.J.K. contributed equally to this work.

[2]To whom correspondence should be addressed. Email: jlee1234@unist.ac.kr.

This article contains supporting information online at www.pnas.org/lookup/suppl/doi:10.1073/pnas.1509674112/-/DCSupplemental.

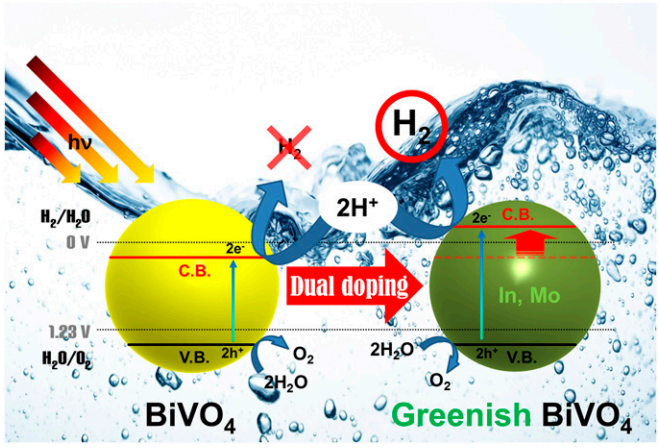

Fig. 1. OWS reaction mechanism by $GBVO_x$.

Split peaks around 35° are merged into one peak as the dopant ratio (x) increases, indicating phase change of $BiVO_4$ from *m* to tetragonal (*t*) (11). Furthermore, Rietveld analysis was performed using X'pert Plus 3.0 software (PANalytical) to determine the fraction of *m*- and *t*-phases as illustrated in Fig. 2*B* and *SI Appendix*, Fig. S2. As the dopant ratio (x in $GBVO_x$) increases, the crystal structure evolves from almost pure *m*-$BiVO_4$ (clinobisvanite; space group: 12/a/(15); JCPDS card no. 014–0688) to a mixture of *m*- and *t*-$BiVO_4$, where *t*-$BiVO_4$ fraction reaches a maximum of 60% at x = 0.10. This doping-induced crystal structure evolution results in unit cell volume growth (Fig. 2*B*) that generates compressive lattice strain, which is discussed in *SI Appendix*, section S4 and visualized in *SI Appendix*, Fig. S1 *E* and *F*. In particular, the compressive lattice strain is the key physical driving force to lift the conduction band of $GBVO_x$ over H^+/H_2 potential (0 V_{RHE} at pH 7), taking collectively both experimental (*SI Appendix*, Fig. S1 *E* and *F*) and theoretical findings (as discussed later).

The UV/Vis (visible) absorption spectra of all samples are shown in Fig. 2*C*. With higher x values of $GBVO_x$, the greater blue shift is observed, indicating that the optical band gap energy of $GBVO_x$ increases with dopant level, whereas the blue shift is not caused by the single Mo doping into $BiVO_4$ (*SI Appendix*, Fig. S4*F*). Actually, the blue shift trend is consistent with the band gap energy transition estimated by extrapolating the linear part of the $(\alpha h\upsilon)^2$- vs. hυ-plot to the energy axis (1) as shown in *SI Appendix*, Fig. S3. According to the Tauc plot, the band gap energy increases from 2.43 eV of pristine $BiVO_4$ to 2.50 eV of $GBVO_{0.10}$. Furthermore, the alteration in the optical band gap energy corresponds to the color evolution of $GBVO_x$ powder samples from yellow to greenish as shown in Fig. 2*C*, *Inset* and *SI Appendix*, Fig. S4. Thus, the ultimate physical driving force for the apparent color evolution is also the compressive lattice strain that widens the band gap by lifting the conduction band. The Mott–Schottky plot in Fig. 2*D* that displays the conduction band of $GBVO_{0.10}$ is elevated to higher than 0 V (vs. RHE at pH 7) by 97.2 mV or ~151 mV from that of pristine $BiVO_4$ (a more clear visualization of the contrast between schematic band structures of pristine $BiVO_4$ and $GBVO_{0.10}$ is in *SI Appendix*, Fig. S5). This finding indicates that photocatalytic water reduction, impossible with pristine $BiVO_4$, becomes possible with $GBVO_{0.10}$, because the dual doping lifts the CBE above the proton reduction potential of 0 V_{RHE} (at pH 7). For the valance band of $GBVO_{0.10}$, it is 81 mV higher than that of pristine $BiVO_4$, but it is still far below the water oxidation potential of 1.23 V_{RHE} (at pH 7) as shown in *SI Appendix*, Fig. S5.

The field emission SEM images in *SI Appendix*, Fig. S6 reveal that all samples consist of irregular polyhedrons of unsystematic size distribution, typical of powder samples synthesized by solid-state reactions. The real atomic ratios in all $GBVO_x$ samples determined by the inductively coupled plasma analysis in *SI Appendix*, Table S1 are close enough to the target values. The high-resolution transmission EM (HR-TEM) and energy-dispersive X-ray spectroscopy elemental mapping in *SI Appendix*, Figs. S6–S10 show that Bi, V, In, and Mo are homogeneously distributed within the $GBVO_x$ particle. All of these characterization results univocally prove that In^{3+} and Mo^{6+} have been effectively inserted into the $BiVO_4$ lattice. The HR-TEM image in *SI Appendix*, Fig. S9*F* illustrates the lattice spacing of 0.450 nm corresponding to the interplanar spacing of the (040) plane of $GBVO_{0.10}$. XPS binding energies in *SI Appendix*, Fig. S11 indicate that the involved elements are all in their stable oxidation states of Bi^{3+}, V^{5+}, Mo^{6+}, and In^{3+}.

OWS Under Visible Light. The OWS reaction was carried out under visible light irradiation (λ ≥ 420 nm; 500-W Hg-arc lamp) with 0.3 g photocatalyst powder dispersed in 100 mL distilled water at pH 7. In phase I shown in Fig. 3, $GBVO_{0.10}$ (the most active $GBVO_x$) showed stoichiometric H_2/O_2 evolution even without modification by any cocatalyst. Hence, the $GBVO_x$ can split pure water by visible light-driven OWS without any sacrificial reagents or additives. In particular, this phenomenon represents the first example, to our knowledge, of a pure water-splitting photocatalyst responding to visible light without any metal cocatalyst. Next, we purged the system with N_2 and tested the OWS reaction after photodepositing 3 wt% RuO_2 on $GBVO_{0.10}$ as a cocatalyst. The photocatalytic activity was significantly improved by adding an RuO_2 cocatalyst that collects electrons/holes and provides active sites for catalytic water reduction and/or oxidation. The other common cocatalysts, such as Pt, Rh, $Rh_xCr_yO_3$, and $Pt_xCr_yO_3$ (4–6), were much less effective on $GBVO_{0.10}$. Phases II–IV present repeated runs of the same catalysts to show the stability of $GBVO_{0.10}$. In phase V, heat treatment (623 K in air for 1 h) further intensified the photocatalytic activity of RuO_2-cocatalyzed $GBVO_{0.10}$. This treatment was aimed at converting the photodeposited $RuO_2 \bullet xH_2O$ on $GBVO_{0.10}$ into the more stable and active form of cocatalyst (i.e., RuO_2) (30).

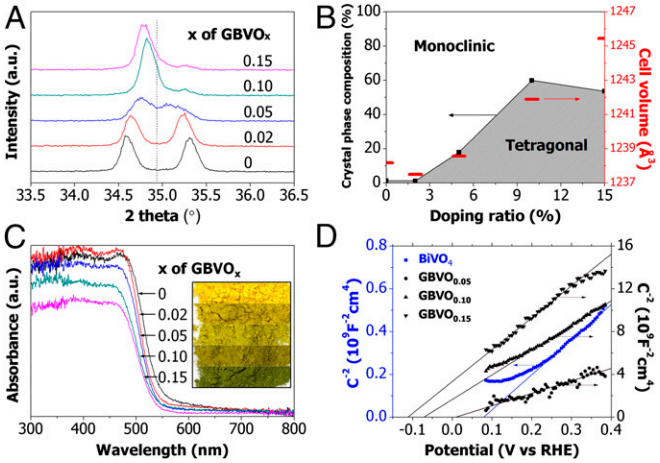

Fig. 2. Photophysical characterization of $GBVO_x$. (*A*) Magnified view of powder XRD patterns of pristine $BiVO_4$ and all $GBVO_x$ samples. (*B*) Crystal-phase diagram with calculated unit cell volume for different x values of $GBVO_x$. (*C*) UV/Vis absorption spectra of pristine $BiVO_4$ and all $GBVO_x$ samples. *Inset* shows color change of the samples. (*D*) Mott–Schottky plot of pristine $BiVO_4$, $GBVO_{0.05}$, $GBVO_{0.10}$, and $GBVO_{0.15}$.

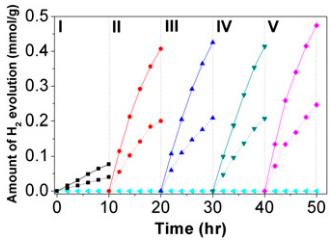

Fig. 3. OWS by $GBVO_{0.10}$ under the visible light ($\lambda \geq 420$ nm) irradiation. Solid and dashed lines indicate evolved H_2 and O_2, respectively. Baseline represents a control experiment by pristine $BiVO_4$. Phase I, unmodified $GBVO_{0.10}$; phases II–IV, 3 wt% $RuO_2/GBVO_{0.10}$; phase V, heat treated 3 wt% $RuO_2/GBVO_{0.10}$.

The rate of hydrogen evolution (~17 μmol h^{-1}) from this 3 wt% RuO_2 on $GBVO_{0.10}$ could be compared with that of the best-known example [~56 μmol h^{-1}; i.e., 5 wt% RuO_2-loaded $(Ga_{1-x}Zn_x)(N_{1-x}O_x)$ under visible light irradiation ($\lambda \geq 400$ nm; 450-W Hg-arc lamp)] (5). The activity of our photocatalyst corresponds to an apparent quantum yield of 3.2% under overall visible light (420–800 nm) irradiation, which was calculated from the amount of evolved hydrogen and photon flux measured by chemical actinometry with ferrioxalate (*SI Appendix*, section S3). The value is also compared with 5.9% at 420–440 nm for $(Ga_{1-x}Zn_x)(N_{1-x}O_x)$ photocatalysts (31). Considering that we used a longer wavelength filter ($\lambda \geq 420$ nm), we can state that the photocatalytic activity of $GBVO_{0.10}$ is comparable with that of the best-known $(Ga_{1-x}Zn_x)(N_{1-x}O_x)$ photocatalyst. However, this work represents the first report, to our knowledge, of visible light-driven OWS over modified $BiVO_4$ in pure water of pH 7 without cocatalyst. This work also represents the first, to our knowledge, OWS photocatalyst based on d(0) electron configuration (V^{5+}), whereas $(Ga_{1-x}Zn_x)(N_{1-x}O_x)$ is made of d(10) configuration (Zn^{2+} and Ga^{3+}). The incident photon to current conversion efficiency was measured for unmodified $GBVO_{0.10}$ film (details are in *SI Appendix*, section S2). As shown in *SI Appendix*, Fig. S12, incident photon to current conversion efficiency of 0.5–2% is observed in 350–480 nm, with the shape of its curve well reflecting the absorption spectrum in Fig. 2*C*. It confirms that the photoresponse of the material corresponds to light absorption by the band to band transition (Fig. 3).

To understand the nature of the photocatalytic water splitting with $GBVO_x$ in more detail, its half reactions were studied in the presence of sacrificial reagents. Namely, Ag^+ ions from $AgNO_3$ act as electron scavengers, and CH_3OH acts as a hole scavenger:

$$2H_2O(l) + h\nu + 4Ag^+ \rightarrow O_2(g) + 4H^+ + 4Ag^0 \text{ and}$$

$$H_2O(l) + h\nu + CH_3OH \rightarrow 3H_2(g) + CO_2(g).$$

In *SI Appendix*, Fig. S13*A*, O_2 evolution rates increased greatly with the single Mo doping ($BiV_{0.98}Mo_{0.02}O_4$). This increase is because of the improved charge transfer properties of $BiVO_4$ as reported earlier (21). However, the dual-metal doping improved the water oxidation activity much further, showing a maximum at the low doping level of $GBVO_{0.02}$. According to the numerical data from *SI Appendix*, Fig. S13*A*, $GBVO_{0.02}$ has dramatically increased photocatalytic water oxidation activity by factors of about 20 and 5 relative to pristine $BiVO_4$ and single-doped $BiV_{0.98}Mo_{0.02}O_4$, respectively. *SI Appendix*, Fig. S14 shows that the single In doping did not induce any *t*-phase formation. However, it increased the rate of O_2 evolution in $Bi_{0.99}In_{0.01}VO_4$ and reduced the rate at the higher In doping level of $Bi_{0.98}In_{0.02}VO_4$.

As *SI Appendix*, Fig. S13*B* exhibits, the effects of doping on H_2 evolution were quite different from those of doping on O_2 evolution. Neither the single doping of Mo^{6+} or In^{3+} nor the low level of dual doping (x = 0.02) produced H_2. The optimum doping level for H_2 evolution was found to be x = 0.10. This trend indicates that, when 10% of In^{3+}/Mo^{6+} is inserted into the $BiVO_4$ lattice, the conduction band gains more negative (higher) potential than 0 V_{RHE} (at pH 7) to achieve photocatalytic water reduction. However, even with the appropriate In^{3+}/Mo^{6+} dopant concentration (x = 0.10), the H_2 evolution rate was two orders of magnitude smaller than the O_2 evolution rate. This comparison reveals that water reduction using photogenerated electrons is the rate-determining step in the OWS reaction by $GBVO_{0.10}$. In this sense, the main role of RuO_2 is most likely to provide augmented reaction sites for H_2 evolution (water reduction).

The stability of $GBVO_{0.10}$ is supported by *SI Appendix*, Fig. S15*C*, revealing no difference in the XRD patterns of $GBVO_{0.10}$ before and after the 40-h OWS reaction. The stability is also confirmed by the turnover number of RuO_2 loaded on $GBVO_{0.10}$ (number of hydrogen atoms produced/number of Ru atoms in RuO_2 as discussed in *SI Appendix*, section S4). The turnover number is estimated to be 11 during the OWS reaction phases II–IV shown in Fig. 3, guaranteeing sustainable catalytic cycles on $GBVO_{0.10}$. However, at 15% In^{3+}/Mo^{6+} dopant concentration ($GBVO_{0.15}$), the crystal structure is damaged after a 40-h OWS reaction, which is shown in *SI Appendix*, Fig. S15*C*. This inferior crystal structure stability of $GBVO_{0.15}$ is most likely caused by the too high In^{3+}/Mo^{6+} dopant concentration of 15%. According to the volumetric strain method and the Williamson–Hall method discussed in *SI Appendix*, Figs. S1 *E* and *F* and S5, the CBE position is proportional to the compressive (minus) lattice stain up to 10% dopant concentration. However, the proportional relation is not valid anymore at 15% dopant concentration because of the inferior crystal structure stability at the too high In^{3+}/Mo^{6+} doping ratio.

First Principle DFT Calculations. Collectively taking into account all of the experimental results from a wide array of instruments and methods, this study has found that there is a significant positive correlation between the compressive (minus) lattice strain and the CBE at least up to 10% In^{3+}/Mo^{6+} dopant concentration. This positive correlation provides the physical driving force to transform (only) O_2-evolving yellow $BiVO_4$ into (both) H_2/O_2-evolving $GBVO_x$ by lifting the CBE, widening the band gap, and entailing the apparent color change. This finding based on a variety of experimental outcomes is also corroborated by the theoretical study using DFT calculations as follows.

The effect of In^{3+}/Mo^{6+} dual doping was investigated by first principle DFT electronic structure calculation on scheelite type *m*-$BiVO_4$ (space group: I2/a) and *t*-$BiVO_4$ (space group: I41/amd). The detailed calculation procedures were based on those described in previous studies (1, 32). The lattice constants as well as atomic coordinates were simultaneously optimized, and the obtained lattice parameters for a conventional cell were a = 7.306 Å, b = 11.747 Å, c = 5.167 Å, and β = 135.003° for *m*-$BiVO_4$ and a = b = 7.307 Å and c = 6.587 Å for *t*-$BiVO_4$. To study the effect of In^{3+}/Mo^{6+} substitution into Bi^{3+}/V^{5+} sites, we used 96-atom $BiVO_4$ host supercell of 2a × b × 2c and conventional cell of $\sqrt{2}$a × $\sqrt{2}$b × 2c for *m*-$BiVO_4$ and *t*-$BiVO_4$, respectively. We examined a single pair of In and Mo atoms' substitution (i.e., the doping concentration x = 0.0625 in $BiVO_4$). The calculated electronic density of states is shown in Fig. 4, where the origin of energy is set to be the valence band edge (VBE) of pristine *m*-$BiVO_4$. The energy levels of *m*-$BiVO_4$ and *t*-$BiVO_4$ with and without doping are effectively compared by aligning the deep-lying O 2s orbital levels.

For *m*-$BiVO_4$, the calculated band gap energy is 2.02 eV without doping and 1.84 eV with doping. This calculation means that the band gap is slightly narrowed on doping. The VBE of doped *m*-$BiVO_4$ is at the same energy level as that of pristine

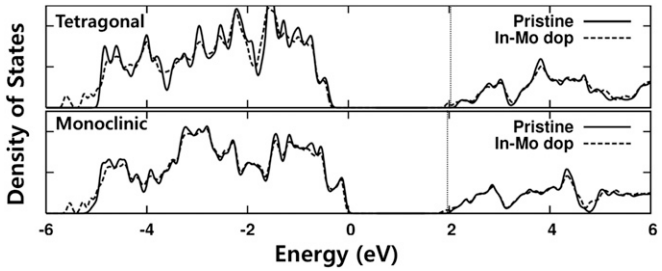

Fig. 4. Density of states of the *t*-$BiVO_4$ and *m*-$BiVO_4$ system with and without In^{3+}/Mo^{6+} dual doping. The energy levels in different structures are aligned comparing the deep-lying oxygen 2s orbital. The Fermi level of In^{3+}/Mo^{6+} doped structure is near CBE, which is shown with vertical dotted lines. The VBE in *t*-structure is −0.32 eV lower than in *m*-$BiVO_4$. In each crystal structure, doping causes band gap narrowing.

m-$BiVO_4$, and the CBE is 0.18 eV lower than pristine *m*-$BiVO_4$. Both of these calculations are contradictory to the experimental findings of increased band gap energy and higher CBE induced by In^{3+}/Mo^{6+} doping. In the case of *t*-$BiVO_4$, the band gap in the equilibrium cell volume is 2.47 eV without doping and 2.31 eV with dual doping. Although the band gap of *t*-$BiVO_4$ is larger (∼0.45 eV) than that of *m*-$BiVO_4$, the CBE is slightly higher (∼0.13 eV) than its counterpart, because the average electronic potential is deeper (work function is higher) in *t*-$BiVO_4$ compared with in *m*-$BiVO_4$. Like *m*-$BiVO_4$ mentioned above, the band gap of *t*-$BiVO_4$ narrows upon doping, and the CBE of doped *t*-$BiVO_4$ is slightly lower than that of pristine *m*-$BiVO_4$, which is also contradictory to the experimental results.

This apparent inconsistency between calculation and experiments can be solved by considering the partial phase change of *m*-$BiVO_4$ to *t*-$BiVO_4$ on dual doping. Indeed, the best-performance water splitter, $GBVO_{0.10}$, contains ∼60% of *t*-phase (Fig. 2*B*). Because the synthesized $GBVO_x$ crystal has the mixed structure of varying fraction *m*- and *t*-phases with respect to the doping concentration, each crystal structure would not have its equilibrium lattice constants. The conventional cell volume of *t*-$BiVO_4$ (351.68 $Å^3$) containing four $BiVO_4$ units is quite larger than that of *m*-$BiVO_4$ (313.54 $Å^3$). The energy-level alignment and the total energy variation of *m*-$BiVO_4$ and *t*-$BiVO_4$ are illustrated with respect to the cell volume in Fig. 5. For doped *m*-$BiVO_4$ with larger cell volume, the band gap is smaller than that of pristine *m*-$BiVO_4$ with the equilibrium lattice constants. Thus, only the energy-level alignment of *t*-$BiVO_4$ is compared with the CBE and VBE of pristine *m*-$BiVO_4$, as shown in Fig. 5*A*. According to the comparison, compressed *t*-$BiVO_4$ with In^{3+}/Mo^{6+} substitution has larger band gap energy as well as higher CBE position than pristine *m*-$BiVO_4$.

This DFT calculation outcome supports the experimental finding of higher CBE. To be more specific, In^{3+}/Mo^{6+} substitution causes partial phase transformation from pure *m*-$BiVO_4$ to a mixture of *m*-$BiVO_4$ and *t*-$BiVO_4$, and the phase transformation results in unit cell volume growth and compressive lattice strain increase. As a result of the compressive lattice strain increase, $GBVO_{0.10}$ (having the optimum mixed crystal structure of ∼60% *t*-$BiVO_4$ and ∼40% *m*-$BiVO_4$ to maximize the compressive lattice strain) can take advantage of uplifted conduction band edge to achieve OWS under visible light without any additives. The physical mechanism on how In^{3+}/Mo^{6+} dual doping triggers the partial phase transformation from pure *m*-$BiVO_4$ to a mixture of *m*-$BiVO_4$ and *t*-$BiVO_4$ is investigated in the following discussion.

To figure out the physical reason why *t*-phase expands as doping concentration grows, we estimated the total energy of each case as shown in Fig. 5*B*. Based on the total energy values, we could also estimate the formation energy of In^{3+}/Mo^{6+} dual dopants within *m*-$BiVO_4$ and *t*-$BiVO_4$ according to the cell volume by calculating the total energy differences between pristine $BiVO_4$ and doped $BiVO_4$. There is no ambiguity to determine the chemical potentials, because the contributions of cation chemical potentials are compensated. The formation energy of In^{3+}/Mo^{6+} dopants in *m*-$BiVO_4$ is about 1.31 eV and independent of lattice strain, but that in *t*-$BiVO_4$ strongly depends on cell volume variation. The formation energy of In^{3+}/Mo^{6+} dopants in *t*-$BiVO_4$ is 1.79 eV in its equilibrium cell volume (1,407 $Å^3$), which is about 0.48 eV higher than that in *m*-$BiVO_4$ at 1,253 $Å^3$. However, as the cell volume goes down, the formation energy of In^{3+}/Mo^{6+} dopants in *t*-$BiVO_4$ decreases and eventually gets smaller than that in *m*-$BiVO_4$ when the cell volume is smaller than ∼1,320 $Å^3$. In addition, the total energy of doped *t*-$BiVO_4$ gets smaller than that of undoped *t*-$BiVO_4$ when the cell volume is smaller than 1,254 $Å^3$. This tendency suggests that, as the cell volume becomes smaller and smaller, the formation of In^{3+}/Mo^{6+} dopants is more promoted within *t*-$BiVO_4$ rather than within *m*-$BiVO_4$, and ultimately, the compressed *t*-crystal structure can be more stabilized with doping than without doping. This doping-induced phase change and the subsequent rise of the CBE

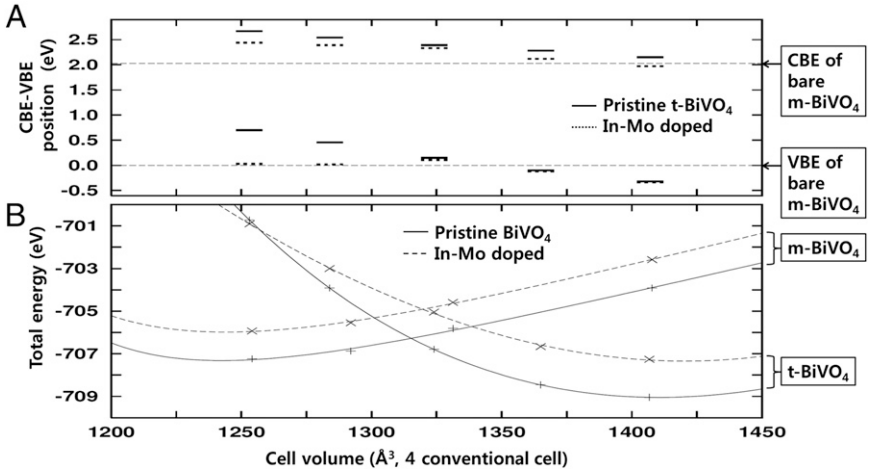

Fig. 5. (*A*) Cell volume dependency of CBE and VBE positions in *t*-$BiVO_4$ systems. The horizontal dashed lines indicate corresponding energy positions in pristine *m*-$BiVO_4$. (*B*) Total energy vs. cell volume plot of *m*-$BiVO_4$ and *t*-$BiVO_4$. The points are calculation results, and the lines stand for the Birch fit to the equation of state.

represent a new concept to create a visible light-active OWS photocatalyst by the band structure engineering.

In summary, through In^{3+}/Mo^{6+} dual doping into the host lattice of m-$BiVO_4$, we have created a new visible light-responsive OWS photocatalyst. The resulting $GBVO_x$ splits water into H_2 and O_2 by one-step photoexcitation, because it has an upshifted CBE transforming (only) O_2-evolving yellow $BiVO_4$ into (both) H_2/O_2-evolving $GBVO_x$, a one-photon OWS photocatalyst. The DFT calculation indicates that In^{3+}/Mo^{6+} dual doping triggers partial phase transformation from pure m-$BiVO_4$ to a mixture of m-$BiVO_4$ and t-$BiVO_4$, which sequentially leads to unit cell volume growth, compressive lattice strain increase, conduction band edge uplift, and band gap widening. This domino effect is also corroborated experimentally. The $GBVO_x$ is an active and stable one-photon OWS photocatalyst made of earth-abundant elements and works in pure water without any additives.

Materials and Methods

Sample Preparation. Powder samples of $GBVO_x$ were prepared by solid-state reaction. Each stoichiometric amount of bismuth oxide (Aldrich; 99.999%), vanadium oxide (Aldrich; 98%), indium oxide (Alfa Aeser; 99.9%), and molybdenum oxide (Aldrich; 99.99%) was mixed well by grinding in an agate mortar and manually pelletized under 2,500 psi. All pellets were preheated at 873 K for 5 h, and then, they were vigorously reground and manually repelletized as mentioned earlier. These pellets were heated again at 1,073 K for 3 h. After this main heating, they were thoroughly reground to get powder samples.

Modification of $GBVO_{0.10}$ with RuO_2. $GBVO_{0.10}$ was modified by photodepositing 3 wt% RuO_2 (the loading had been optimized). Specifically, the photodeposition was carried out at room temperature under atmospheric pressure in a closed Pyrex glass vessel containing nitrogen-purged suspension of $GBVO_{0.10}$ powder and $RuCl_36H_2O$ in 50 mL methanol and 50 mL distilled water under visible light irradiation for 8 h. The light source was an Hg-arc lamp (500 W; Oriel) equipped with a UV cutoff filter ($\lambda \geq 420$ nm). After this photodeposition, RuO_2-loaded $GBVO_{0.10}$ was vacuum-filtered, washed with distilled water, and dried in an air oven at 70 °C for 12 h. Finally, the dried powder sample was heated at 623 K for 1 h.

Physicochemical Characterization. The structural properties of $GBVO_x$ were investigated by using powder XRD (X'pert Pro; Phillips). Rietveld analysis was performed using X'pert Plus 3.0 software (PANalytical) to calculate the phase ratios of m-structure to t-structure in $GBVO_x$. The UV-visible diffuse reflectance spectra were measured with a UV-visible spectrometer (UV-2401PC; Shimadzu Co.) equipped with integrated sphere method. The particle size and morphology were examined by field emission SEM (JEOL JSM-6330F). The HR-TEM images, high-angle annular dark field images, and corresponding elemental mapping images were obtained by using Cs-corrected high-resolution scanning transmission EM (JEM 2200FS; 200 kV; JEOL) at the National Research Center for Nanomaterial Technology at Pohang University of Science and Technology in Korea. The atomic ratios of bismuth to indium and vanadium to molybdenum in $GBVO_x$ were analyzed by using inductively coupled plasma.

Photocatalytic Activity Measurement Under Visible Light Irradiation. The structural properties of $GBVO_x$ were investigated by using powder XRD. The photocatalytic activities under visible light were investigated by measuring H_2 and O_2 evolution at room temperature under atmospheric pressure in a closed Pyrex glass vessel (193.5, 187, and 189 mL) containing nitrogen-purged suspension of 0.3 g photocatalyst powder in 100 mL distilled water. The light source was an Hg-arc lamp (450 W; Oriel) equipped with a UV cutoff filter ($\lambda \geq 420$ nm). The evolved amounts of H_2 and O_2 were analyzed by a gas chromatograph (HP5890) with a thermal conductivity detector and a molecular sieve 5-A column.

ACKNOWLEDGMENTS. We thank N. H. Ahn (Pohang University of Science and Technology) for assistance with collecting X-ray diffraction data. W.J.J. thanks the Samsung Foundation of Culture for a Samsung Scholarship. This work was supported by the Brain Korea Plus Program of the Ministry of Education, Korean Centre for Artificial Photosynthesis Grant 2009-0093880, the Ministry of Trade, Industry and Energy of Republic of Korea Project 10050509, and the Ulsan National Institute of Science and Technology. This work was also supported, in part, by the US Army Research Laboratory and the US Army Research Office through Institute for Soldier Nanotechnologies Contract W911NF-13-D-0001.

1. Jo WJ, et al. (2012) Phosphate doping into monoclinic $BiVO_4$ for enhanced photoelectrochemical water oxidation activity. *Angew Chem Int Ed Engl* 51(13):3147–3151.
2. Grätzel M (2005) Solar energy conversion by dye-sensitized photovoltaic cells. *Inorg Chem* 44(20):6841–6851.
3. Bard AJ, Fox MA (1995) Artificial photosynthesis: Solar splitting of water to hydrogen and oxygen. *Acc Chem Res* 28(3):141–145.
4. Maeda K, et al. (2006) Photocatalyst releasing hydrogen from water. *Nature* 440(7082):295.
5. Maeda K, et al. (2005) GaN:ZnO solid solution as a photocatalyst for visible-light-driven overall water splitting. *J Am Chem Soc* 127(23):8286–8287.
6. Chen X, Liu L, Yu PY, Mao SS (2011) Increasing solar absorption for photocatalysis with black hydrogenated titanium dioxide nanocrystals. *Science* 331(6018):746–750.
7. Liu H, et al. (2011) Novel photocatalyst of V-based solid solutions for overall water splitting. *J Mater Chem* 21(41):16535–16543.
8. Wang D, et al. (2012) Photocatalytic water oxidation on $BiVO_4$ with the electrocatalyst as an oxidation cocatalyst: Essential relations between electrocatalyst and photocatalyst. *J Phys Chem C* 116(8):5082–5089.
9. Kudo A, Omori K, Kato H (1999) A novel aqueous process for preparation of crystal form-controlled and highly crystalline $BiVO_4$ powder from layered vanadates at room temperature and its photocatalytic and photophysical properties. *J Am Chem Soc* 121(49):11459–11467.
10. Tokunaga S, Kato H, Kudo A (2001) Selective preparation of monoclinic and tetragonal $BiVO_4$ with scheelite structure and their photocatalytic properties. *Chem Mater* 13(12):4624–4628.
11. Hong SJ, Lee S, Jang JS, Lee JS (2011) Heterojuction $BiVO_4/WO_3$ electrodes for enhanced photoactivity of water oxidation. *Energy Environ Sci* 4(5):1781–1787.
12. Yao W, Iwai H, Ye J (2008) Effects of molybdenum substitution on the photocatalytic behavior of $BiVO_4$. *Dalton Trans* (11):1426–1430.
13. Long M, Cai W, Kisch H (2008) Visible light induced photoelectrochemical properties of n-$BiVO_4$ and n-$BiVO_4$/p-$Co3O_4$. *J Phys Chem C* 112(2):548–554.
14. Jiang HQ, Endo H, Natori H, Nagai M, Kobayashi K (2009) Fabrication and efficient photocatalytic degradation of methylene blue over CuO/$BiVO_4$ composite under visible-light irradiation. *Mater Res Bull* 44(3):700–706.
15. Kim TW, Choi K-S (2014) Nanoporous $BiVO_4$ photoanodes with dual-layer oxygen evolution catalysts for solar water splitting. *Science* 343(6174):990–994.
16. Kohtani S, Tomohiro M, Tokumura K, Nakagaki R (2005) Photooxidation reactions of polycyclic aromatic hydrocarbons over pure and Ag-loaded $BiVO_4$ photocatalysts. *Appl Catal B* 58(3-4):265–272.
17. Kohtani S, et al. (2005) Adsorptive and photocatalytic properties of Ag-loaded $BiVO_4$ on the degradation of 4-*n*-alkylphenols under visible light irradiation. *Catal Commun* 6(3):185–189.
18. Yao W, Ye J (2006) Photophysical and photocatalytic properties of $Ca_{(1-x)}Bi_xV_xMo_{(1-x)}O_4$ solid solutions. *J Phys Chem B* 110(23):11188–11195.
19. Luo W, et al. (2011) Solar hydrogen generation from seawater with a modified $BiVO_4$ photoanode. *Energy Environ Sci* 4(10):4046–4051.
20. Parmar KPS, et al. (2012) Photocatalytic and photoelectrochemical water oxidation over metal-doped monoclinic BiVO(4) photoanodes. *ChemSusChem* 5(10):1926–1934.
21. Asahi R, Morikawa T, Ohwaki T, Aoki K, Taga Y (2001) Visible-light photocatalysis in nitrogen-doped titanium oxides. *Science* 293(5528):269–271.
22. Park HS, et al. (2011) Factors in the metal doping of $BiVO_4$ for improved photoelectrocatalytic activity as studied by scanning electrochemical microscopy and first-principles density-functional calculation. *J Phys Chem C* 115(36):17870–17879.
23. Wang Q, Liu H, Yuan J, Shangguan W (2009) Synthesis and characterization of visible-light-responding $Bi_{0.5}La_{0.5}VO_4$ solid solution for photocatalytic water splitting. *Chin J Catal* 30(6):565–569.
24. Sasaki Y, Nemoto H, Saito K, Kudo A (2009) Solar water splitting using powdered photocatalysts driven by Z-schematic inter-particle electron transfer without an electron mediator. *J Phys Chem C* 113(40):17536–17542.
25. Seabold JA, Zhu K, Neale NR (2014) Efficient solar photoelectrolysis by nanoporous Mo:BiVO4 through controlled electron transport. *Phys Chem Phys* 16(3):1121–1131.
26. Park Y, McDonald KJ, Choi K-S (2013) Progress in bismuth vanadate photoanodes for use in solar water oxidation. *Chem Soc Rev* 42(6):2321–2337.
27. Zhong DK, Choi S, Gamelin DR (2011) Near-complete suppression of surface recombination in solar photoelectrolysis by "Co-Pi" catalyst-modified W:BiVO4. *J Am Chem Soc* 133(45):18370–18377.
28. Abdi FF, Krol RVD (2012) Nature and light dependence of bulk recombination in Co-Pi-catalyzed $BiVO_4$ photoanodes. *J Phys Chem C* 116(17):9398–9404.
29. Abdi FF, Savenije TJ, May MM, Dam B, Krol RVD (2013) The origin of slow carrier transport in $BiVO_4$ thin film photoanodes: A time-resolved microwave conductivity. *J Phys Lett* 4(16):2752–2757.
30. Mills A, Lee S-K (2003) Platinum group metals and their oxides in semiconductor photosensitization. *Platin Met Rev* 47(1):2–12.
31. Maeda K, Teramura K, Domen K (2008) Effect of post-calcination on photocatalytic activity of $(Ga_{1-x}Zn_x)(N_{1-x}O_x)$ solid solution for overall water splitting under visible light. *J Catal* 254(2):198–204.
32. Yin WJ, Wei SH, Al-Jassim MM, Turner J, Yan Y (2011) Doping properties of monoclinic BiVO4 studied by first-principles density-functional theory. *Phys Rev B* 83(15): 1–11.